Charge carrier transport with low-temperature anomalies in engineered $4d/5d$ oxide superlattices of $(Sr_2IrO_4)_4/(Sr_3Ru_2O_7)_N$

Hui Xu,[1] Alexander J. Grutter,[2] Zhangzhang Cui,[1] Zhicheng Wang,[1] Xiaofang Zhai,[1,3,*] and Yalin Lu[1,4,†]

[1]*Hefei National Laboratory for Physical Sciences at the Microscale, University of Science and Technology of China, Hefei 230026, China*

[2]*NIST Center for Neutron Research, National Institute of Standards and Technology, Gaithersburg, Maryland 20899, USA*

[3]*School of Physical Science and Technology, ShanghaiTech University, Pudong, Shanghai 201210, China*

[4]*Synergy Innovation Center of Quantum Information and Quantum Physics, University of Science and Technology of China, Hefei, Anhui 230026, China*

(Received 17 December 2019; revised manuscript received 31 March 2020; accepted 7 April 2020; published 30 April 2020)

We report the tunable conducting behavior of a series of $(Sr_2IrO_4)_4/(Sr_3Ru_2O_7)_N$ ($N = 1$, 2, and 4) atomic layer superlattices, in which phases of itinerant electrons, itinerant holes, localized electrons, and an anomalous charge region can be varied dependent on the period and the temperature. Specifically, for the $N = 4$ superlattice, the electron-to-hole transition occurs at a temperature of 35 K, at which the sample behaves as an intrinsic insulator without either electrons or holes. Upon further reducing the temperature to below 16 K, the superlattice enters an anomalous phase region in which an abrupt zero-to-negative magnetoresistance transition and a Hall resistivity kink are observed at 1.3 and 2.1 T, respectively. Above these fields, polarized neutron reflectivity measurements revealed ferromagnetism confined in the $Sr_3Ru_2O_7$ layers. Moreover, the $N = 2$ superlattice exhibits a bump feature in the anomalous Hall resistivity near 1.3 T, which is similar to the previously reported topological Hall phenomenon in ultrathin $SrRuO_3$ heterostructures. We demonstrate that the layered $4d/5d$ oxide superlattice is a powerful platform in engineering exotic types of phases which have not been explored in their thin-film or bulk samples.

DOI: 10.1103/PhysRevB.101.155151

I. INTRODUCTION

Interface engineering has long played a key role in manipulating the electronic state in $3d$ transition-metal oxides, which has led to exotic phenomena such as the two-dimensional electron gas in $LaAlO_3/SrTiO_3$ [1]. In recent years, the $4d$ and $5d$ heavy transition-metal oxides have attracted considerable attention due to their strong spin-orbit interactions and the consequent resulting exotic phases, such as the correlated topological insulator and the Weyl semimetal [2–5]. Among them, the layered Ruddlesden-Popper oxides of $A_{n+1}B_mO_{3n+1}$ (A is the rare or alkali earth element and B is a transition-metal element) show great promise in many aspects. For example, the spin-orbit-coupling–induced high-temperature superconductivity has been predicted to emerge in the $m = 1$ Sr_2IrO_4 under electron doping. The $m = 2$ $Sr_3Ru_2O_7$ has been found to exhibit a quantum metamagnetic transition at low temperatures [6,7]. Despite a great deal of effort applied to exploring these layered oxides, their interfaces have received limited attention. It thus makes the exploration of magnet-electric transports of superlattices (SLs) composed of the layered heavy metal oxides with strong spin-orbit interactions an intriguing task. Here, the SL period may provide a control knob for interfacial proximity effects, while the layered structure narrows the bandwidth yielding an electronic structure more sensitive to SL modulation.

Because of the spin-orbit coupling and the electron correlation effects, the pristine Sr_2IrO_4 thin film exhibits an insulating state with a small gap between the $J_{eff} = 1/2$ upper and lower Hubbard bands [2]. Various experimental approaches have been exploited to convert the insulating state to the metallic or superconducting state [3,8–12]. The $Sr_3Ru_2O_7$ single crystal is a paramagnetic metal at temperatures above 1 K, below which a metamagnetic phase transition occurs due to the Fermi-surface instability under external magnetic fields [13–15]. The $Sr_3Ru_2O_7$ thin film under epitaxial strain exhibits a similar metamagnetic transition but with much enhanced electron nematicity than the single crystal [16]. It is possible to manipulate such a nematic electron state through the interface coupling between the $Sr_3Ru_2O_7$ and Sr_2IrO_4 layers, which may enrich the ongoing exploration of correlated electronic states in the heavy transition-metal oxides.

We fabricated $(Sr_2IrO_4)_4/(Sr_3Ru_2O_7)_N$ SLs with $N = 1$, 2, and 4 on (0 0 1) $SrTiO_3$ and $SrTiO_3$:Nb (0.7 wt % Nb) substrates using pulsed laser deposition (PLD) assisted with high-pressure reflective high-energy electron diffraction (RHEED). In this work, the index N does not represent the number of unit cells but the number of chemical formula units. We note that one unit cell is equal to four chemical formula units in bulk Sr_2IrO_4, and one unit cell is equal to two chemical formula units in bulk $Sr_3Ru_2O_7$. We find that

*Corresponding author: zhaixf@shanghaitech.edu.cn

†Corresponding author: yllu@ustc.edu.cn

the electric transport transits from the localized electron type in the $N = 1$ SL to the itinerant electron type in the $N = 2$ and 4 SLs. Moreover, the itinerant electron transitions to itinerant holes below a critical temperature of 35 K in the $N = 4$ SL. In the diagrams controlled by SL period (N) and temperature, four distinct transport regimes are observed, including regions of localized electrons, itinerant electrons, itinerant holes, and an anomalous region of localized charges. In the anomalous charge phase region, we observe two striking magnetic behaviors, including a rare zero-to-negative magnetoresistance transition ($N = 4$) and a strong anomalous Hall resistivity bump ($N = 2$), both when the field is 1.3 T. The results demonstrate a promising route to tailor the magnetoelectronic phases of heavy 4*d* and 5*d* transition-metal oxides.

II. EXPERIMENT

All samples discussed in this work are approximately 28 nm thick, and one SL period consists of four chemical formula units of Sr_2IrO_4 and N chemical formula units of $Sr_3Ru_2O_7$. We define one bilayer of Sr_2IrO_4 and $Sr_3Ru_2O_7$ as one supercell. For the $N = 1$, 2, 4 SLs, the supercells are repeated 8, 6, and 4 times, respectively. The substrates were etched by buffered hydrofluoric acid and annealed at 950 °C for 1.5 h to obtain the atomically flat TiO_2 termination. During the deposition, one chemical formula unit of Sr_2IrO_4 was identified by one RHEED oscillation period, and one chemical formula unit of $Sr_3Ru_2O_7$ was identified by two RHEED oscillation periods. Such a RHEED-period to chemical-formula-unit conversion was achieved by comparing to x-ray reflectivity (XRR) thickness measurements of Sr_2IrO_4 and $Sr_3Ru_2O_7$ films, respectively. The SLs were deposited with the substrate temperature of 870 °C and oxygen background pressure of 0.3 Pa. The laser energy density was 1.8 J/cm^2 and the repetition rate was 2 Hz using a KrF excimer laser with $\lambda = 248$ nm. All samples were cooled to room temperature with oxygen pressure of 10^4 Pa after growth. The magnetoelectric properties of the SLs, the Sr_2IrO_4 and $Sr_3Ru_2O_7$ films, were measured using a physical property measurement system.

III. RESULTS

A. Structural characterizations

Figures 1(a)–1(c) display the schematic stacking orders of the $(Sr_2IrO_4)_4/(Sr_3Ru_2O_7)_N$ SLs. Figure 1(d) shows the RHEED pattern of a $SrTiO_3$ substrate at 870 °C, and Figs. 1(e)–1(h) show the RHEED patterns of the four consecutive $Sr_3Ru_2O_7$ chemical formula units of the $N = 4$ sample, respectively. We observed only three main diffraction streaks in the above RHEED patterns, which indicate the high quality of the SL growth. We performed the x-ray diffraction (XRD) measurements of all SLs, and the ω-2θ scan results are shown in Fig. 1(i). The (0 0 L) diffractions of SLs and the $SrTiO_3$ substrate are clearly observed, and L is the reciprocal space lattice index along the k_z direction. The L value is calculated using the supercell lattice constant c along the out-of-plane direction, and c is estimated using the bulk $Sr_3Ru_2O_7$ and Sr_2IrO_4 thin-film lattice constants. Then c is derived from the actual SL peak positions in Fig. 1(i) to be 6.67, 4.52, and 3.61 nm for the $N = 4$, 2, and 1 SLs, respectively. The above experimentally derived c values agree well with the estimated c values using the bulk lattice constants of Sr_2IrO_4 (2.57 nm, consisting of four chemical formula units) and $Sr_3Ru_2O_7$ (2.06 nm, consisting of two chemical formula units) films. Furthermore, the thicknesses of the SLs, $Sr_3Ru_2O_7$ and Sr_2IrO_4 films, measured by XRR [shown in Fig. 1(j)] are all approximately 28 nm, in excellent agreement with the designed structure. In addition, we fit the XRR to extract the level of surface/interface roughnesses of the SLs and the bare films. Figure 1(j) shows the model fits, which yield the surface/interface roughnesses of 1.05(±0.04) nm for the SLs, 1.23 (±0.02) nm for the $Sr_3Ru_2O_7$ and Sr_2IrO_4 films with similar thicknesses of 28 nm (see the Supplemental Material (SM) Table S1 [17]). Thus the interfacial roughness level is similar across all SLs and bare films. Additionally, we have measured the reciprocal space maps and the rocking curves of all SLs, which shows that they are fully strained to the substrates and have similar structural qualities (see SM Sec. S1, Sec. S2, and Table S2 [17]).

B. Electrical transport properties

To understand the evolution of the electronic structure with $Sr_3Ru_2O_7$ layer thickness, we performed the electrical transport measurements of the SLs. Figure 2(a) shows the normalized electrical resistivity ρ/ρ (200 K) versus temperature of the $(Sr_2IrO_4)_4/(Sr_3Ru_2O_7)_N$ SLs, $Sr_3Ru_2O_7$ and Sr_2IrO_4 films. Consistent with previous reports [7,16], the Sr_2IrO_4 film shows an insulating behavior and the $Sr_3Ru_2O_7$ film shows a metallic behavior. The dotted lines show the simulated data of the SLs, which was calculated using the parallel resistor model of slabs of four chemical formula units of Sr_2IrO_4 and N chemical formula units of $Sr_3Ru_2O_7$. In the calculation, the model resistivity of each slab was assumed to be the resistivity of the thin films grown under the same condition. It can be clearly seen that the simulated data are inconsistent with the experimental data, with the former being more metallic and absent of localization transitions. Therefore, the proximity effect between the two-component slabs plays a dominant role in causing such differences. In Fig. 2(a) we define T^* as the localization temperature where $d\rho/dT$ changes the sign. The SL resistivity decreases linearly [Fig. 2(b)] with decreasing temperature above T^* of 72, 35, and 16 K for $N = 1$, 2, and 4, respectively, and increases with decreasing temperature below T^*. Previous studies have found that both the bulk $Sr_3Ru_2O_7$ and the electron-doped Sr_2IrO_4 have a linear-T-dependent resistance at high temperatures, consistent with the observed linear-T dependence above T^* [8,18,19]. The conductivity (σ) versus temperature relationships below T^* are further analyzed, as shown in Fig. 2(c). In the low-temperature range, a good linear relationship between σ and the logarithms of temperature (ln$T$) can be observed in Fig. 2(c), in agreement with the localization model in two dimensions [20]. Other models such as the Kondo effect, three-dimensional (3D) variable-range-hopping (VRH) conduction, and two-dimensional (2D) VRH conduction were also examined as shown in SM Sec. S3 [17], but they were inconsistent with the data.

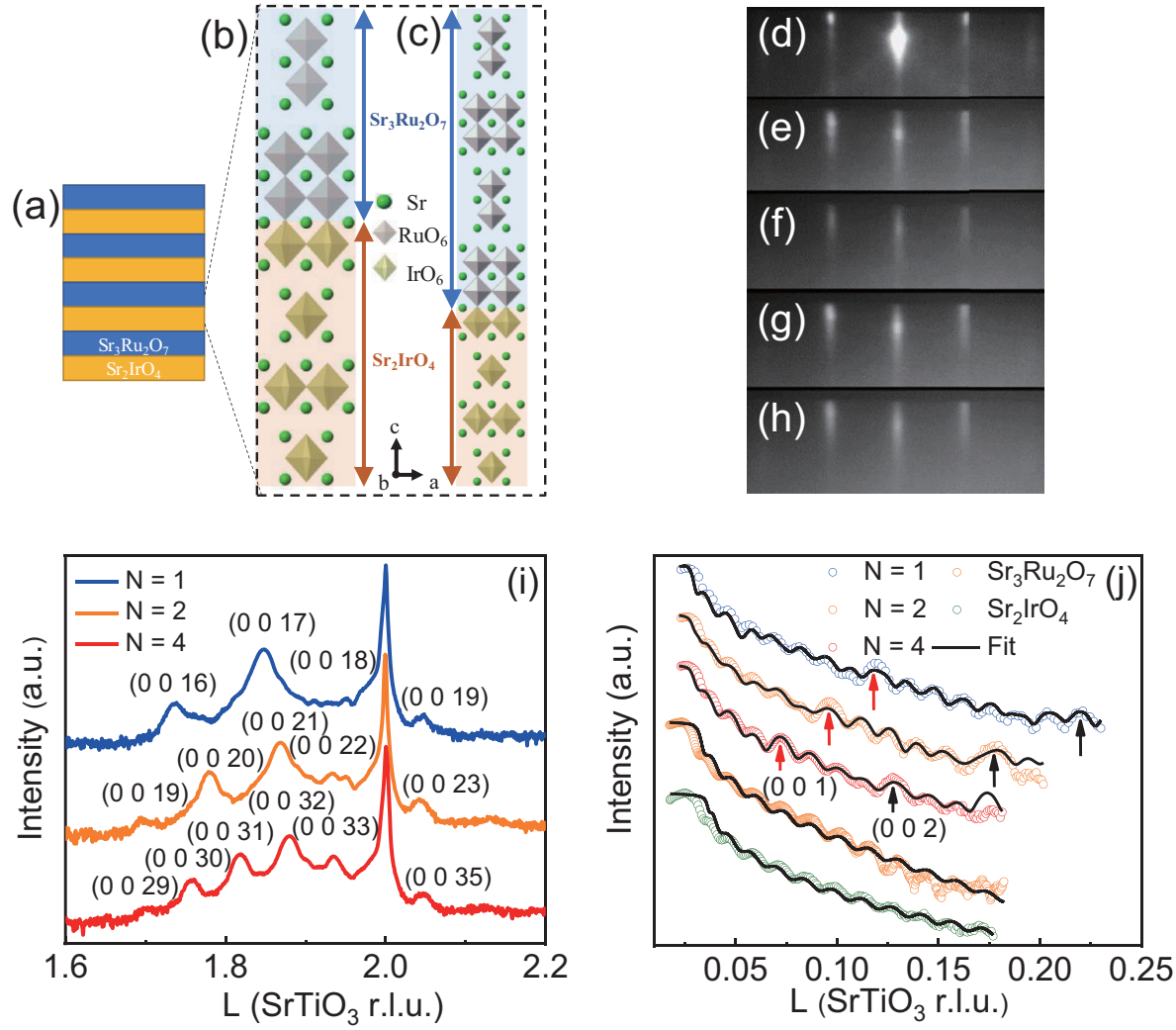

FIG. 1. (a) The stacking of Sr_2IrO_4 and $Sr_3Ru_2O_7$ layers in the $(Sr_2IrO_4)_4/(Sr_3Ru_2O_7)_N$ superlattices (SLs) and the atomic cartoons of (b) $N = 2$ and (c) $N = 4$ SLs. (d)–(h) In-suit reflective high-energy electron diffraction (RHEED) patterns recorded during the $N = 4$ SL growth: (d) $SrTiO_3$ substrate before growth, (e)–(h) after each supercell with $Sr_3Ru_2O_7$ termination layers. (i) The XRD patterns of the SLs measured along the (0 0 L) zone axis; L is calculated using the $SrTiO_3$ substrate lattice constant. (j) XRR of the SLs, Sr_2IrO_4 and $Sr_3Ru_2O_7$ films.

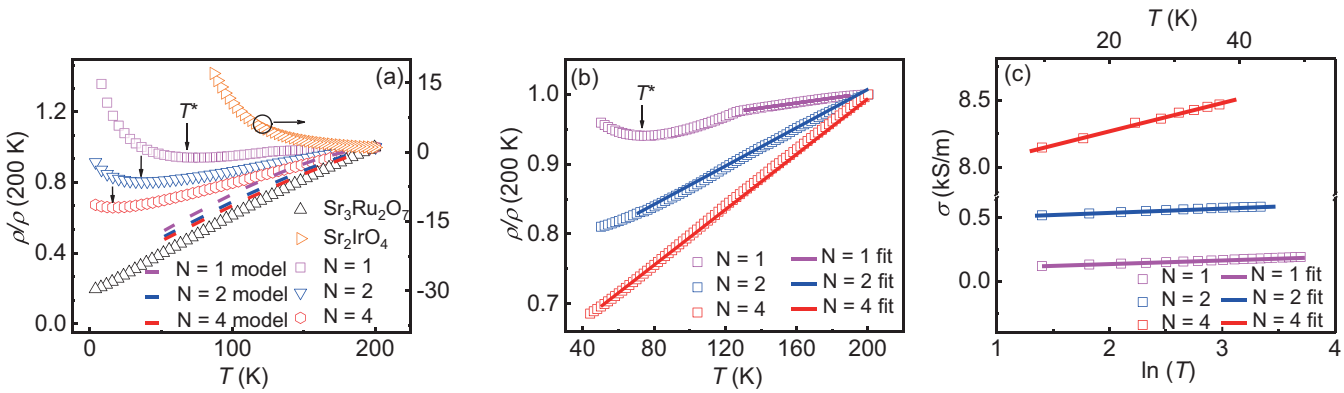

FIG. 2. (a) The normalized resistivity $\rho/\rho(200\,\mathrm{K})$ vs temperature for the SLs, Sr_2IrO_4 and $Sr_3Ru_2O_7$ films. The dashed lines show the calculated resistivity using data of the $Sr_3Ru_2O_7$ and Sr_2IrO_4 films by assuming them as parallel resistors. Arrows mark the localization temperatures T^*. (b) Enlarged view of the measured $\rho/\rho(200\,\mathrm{K})$ of the SLs between 40 and 200 K. (c) The ln T dependence of conductivities in the SLs below the localization temperature T^*. The solid lines in (b) and (c) serve as guides to the eye.

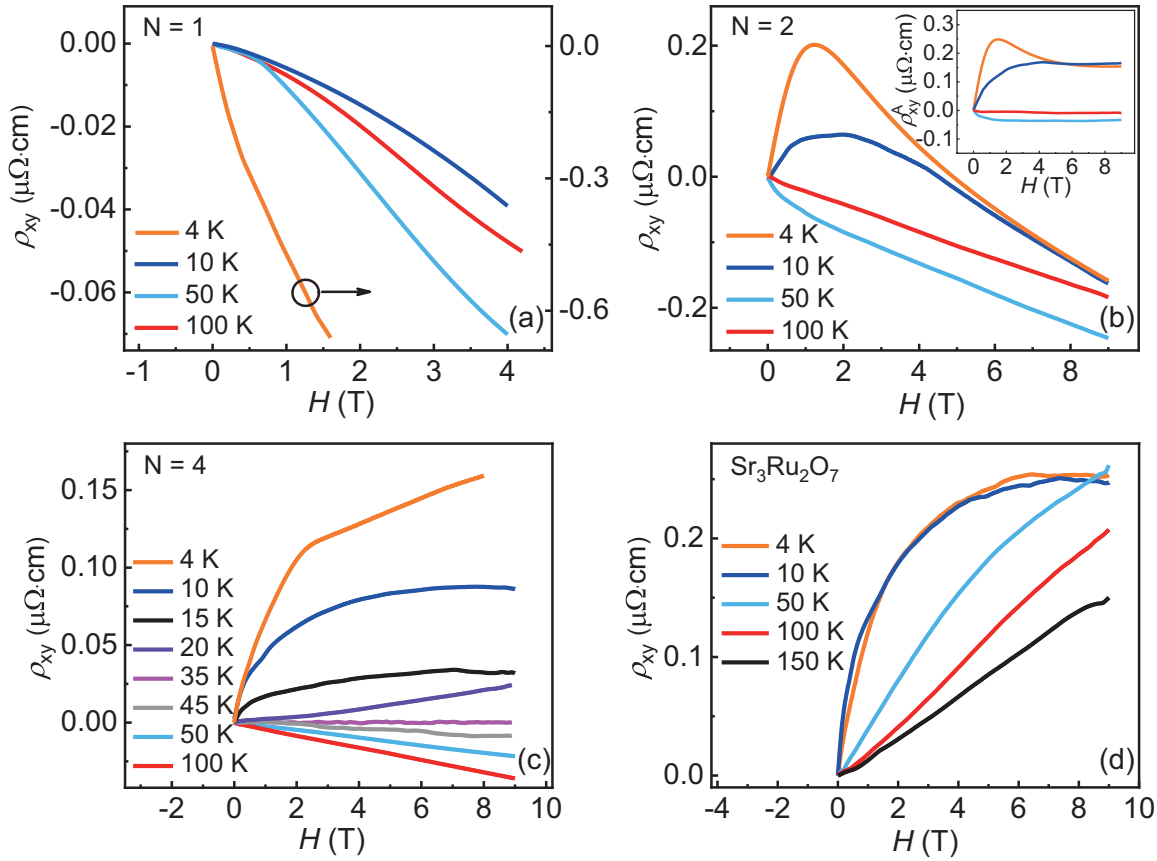

FIG. 3. The magnetic field dependence of Hall resistivity ρ_{xy} of (a)–(c) the $N = 1$, 2, and 4 SLs and (d) the $Sr_3Ru_2O_7$ film measured at various temperatures. Inset in (b): the linear part of Hall resistivity is subtracted from ρ_{xy} data in the main figure of (b).

C. Hall effect measurements and magnetoresistance characterizations

We employed Hall effect measurements to extract the carrier type. The magnetic field dependence of the Hall resistivity ρ_{xy} of the $(Sr_2IrO_4)_4/(Sr_3Ru_2O_7)_N$ SLs and the $Sr_3Ru_2O_7$ film at temperatures between 4 and 100 K are shown in Figs. 3(a)–3(d). In the $N = 1$ SL, the ρ_{xy} slopes are negative across the entire temperature range, corresponding to electrons as the primary charge carriers, in both the metallic (above 72 K) and localized regions (below 72 K) as shown in Fig. 3(a). On the other hand, the $N = 2$ SL exhibits negative slopes (electron carriers) in the metallic regime but more complex behaviors in the localized regime [Fig. 3(b)]. In the low-temperature localized regime, the $N = 2$ slope is initially positive but transitions to a negative slope above 1.3 T. By subtracting the linear Hall resistivity [see inset Fig. 3(b)], a bumplike feature is observed at 4 K near 1.3 T, which resembles the previously reported anomaly in the $SrRuO_3$ ultrathin structures [21]. In Fig. 3(c), the negative-to-positive slope sign transition is found in the $N = 4$ SL across the temperature of 35 K, which is relatively higher than the localization temperature of 16 K. At 4 K, the ρ_{xy} vs H of the $N = 4$ SL shows a kink at a larger field of about 2.1 T, but the anomalous Hall bump is not observed. The linear-field-dependent ρ_{xy} that occurs above the localization temperature can be explained using the electron and hole coexisting picture. The hole carriers are from the $Sr_3Ru_2O_7$ conducting channel, which dominates the $Sr_3Ru_2O_7$ film conductance at all temperatures [see Fig. 3(d)] [13]. The electron carriers are from the Sr_2IrO_4 layers, since SLs with more Sr_2IrO_4 layers are dominated by electron carriers.

Measurements of magnetoresistance have been done to further reveal the nature of the magnetism. Figures 4(a)–4(e) show magnetoresistance (expressed as $[(R(H)–R(0))/R(0)] \times 100\%$ of Sr_2IrO_4, $Sr_3Ru_2O_7$ films and the $N = 1$, 2, and 4 SLs measured with applied field parallel to the c axis. In the testing temperature range from 4 to 150 K, Sr_2IrO_4 thin films exhibit mostly negative magnetoresistance, which increases with decreasing temperature [see Fig. 4(a)] and is consistent with previous reports [22]. $Sr_3Ru_2O_7$ thin films exhibit small negative magnetoresistance at intermediate temperature of 150 K and positive magnetoresistance below about 50 K [see Fig. 4(b)], which is in line with previous reports [16]. As shown in Figs. 4(c)–4(e), the SLs all exhibit a negligibly small positive magnetoresistance at 150 K which is above the ferromagnetic transition temperature of the SLs (also see SM Sec. S4 [17]). The SLs all exhibit negative magnetoresistances with the temperature further reduced. To the lowest testing temperatures of 4 K, negative magnetoresistance is observed in all SLs. Strikingly, at 4 K, in the $N = 4$ SL we observe a zero magnetoresistance to negative magnetoresistance transition near the critical field of 1.3 T. Such a large range zero magnetoresistance has only been observed

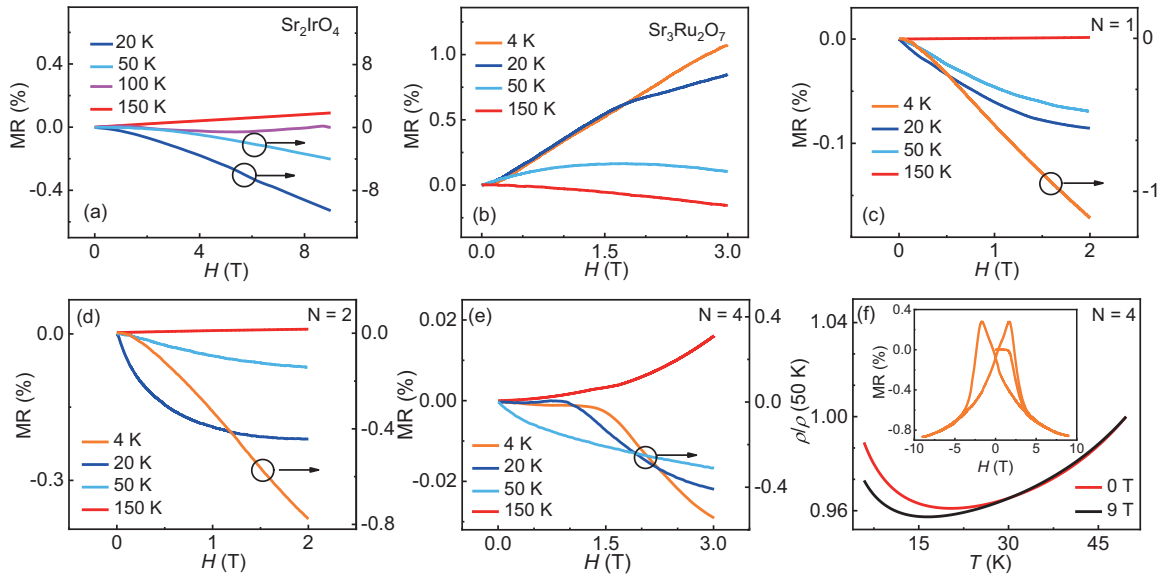

FIG. 4. The magnetic field dependence of magnetoresistance $[R(H)–R(0)]/R(0) \times 100\%$ of the (a) Sr_2IrO_4 and (b) $Sr_3Ru_2O_7$ films, and the (c)–(e) $N = 1$, 2, and 4 SLs at temperatures between 4 and 150 K. (f) The temperature dependence of resistivity in the $N = 4$ SL in the low-temperature range under 0 and 9 T magnetic fields. The inset in (f) shows the hysteresis measurement of the magnetoresistance of the $N = 4$ SL at 4 K.

in graphene before [23]. Furthermore, the continuous temperature-dependent resistivity measured at zero field and 9 T are shown in Fig. 4(f), and the field-dependent magnetoresistance measured at 4 K is shown in the inset of Fig. 4(f), both confirming a ferromagnetic state below the localization temperature.

D. Magnetism measured by polarized neutron reflectivity

The interpretation of the low-temperature anomalies discussed above, including both the abrupt transitions of the Hall resistivity and the magnetoresistance near the critical field, depends critically on the distribution of magnetization within the SLs. A probe that can identify whether the magnetic transitions occur within the Sr_2IrO_4 or the $Sr_3Ru_2O_7$ is therefore required. We addressed this by performing a polarized neutron reflectivity (PNR) measurement on an $N = 4$ SL at 5 K in an applied in-plane field of 3 T using the polarized beam reflectometer instrument at the NIST Center for Neutron Research [24]. PNR is sensitive to the depth profile of the nuclear scattering length density (SLD), which depends on the density and composition of the layers, and, through the neutron dipole moment, the magnetic SLD, which is proportional to the net magnetization. The incident and reflected neutron beams were spin polarized parallel and antiparallel to the applied field, and the reflected intensity was measured as a function of the momentum transfer vector along the film normal (Q_Z). Because of the large applied field, no net in-plane magnetization is expected to lie perpendicular to the applied field so that spin-slip scattering may be neglected. We therefore collected only the non-spin-flip scattering cross sections, R^{++} and R^{--}, which probe in-plane magnetization parallel to the applied field. Data were reduced with the REDUCTUS software program and model fit with REFL1D using a combination of genetic and Markov chain Monte Carlo algorithms for χ^2 optimization as implemented in the BUMPS software package [24,25].

In understanding the results shown in Fig. 5, the key features are the sign and magnitude of the splitting between R^{++} and R^{--} near the critical edge (Q_Z near $0.17\,\mathrm{nm}^{-1}$) and the first-order SL peak (Q_Z near $0.8\,\mathrm{nm}^{-1}$), which is best highlighted through the spin asymmetry, defined as $(R^{++} - R^{--})/(R^{++} + R^{--})$, shown in Fig. 5(b). In particular, the sign of the splitting at the first-order SL peak reverses depending on whether the net magnetization originates in the Sr_2IrO_4 or $Sr_3Ru_2O_7$ layers. We considered a wide variety of models (see SM Sec. S5 and Sec. S6 [17]), which included a uniform magnetization throughout the SL, magnetization confined exclusively to the Sr_2IrO_4, magnetization confined exclusively to the $Sr_3Ru_2O_7$, and varying magnetization on both Sr_2IrO_4 and $Sr_3Ru_2O_7$. Consistently, we found that the only models which are able to properly describe the splitting in the PNR data are those in which most or all of the magnetization is localized within the $Sr_3Ru_2O_7$ layers. PNR therefore demonstrates a magnetization of $-13 \pm 11\,\mathrm{emu/cc}$ ($1\,\mathrm{emu} = 1\mathrm{kA\,m}^2$) in the Sr_2IrO_4 layer but a measurable ferromagnetism of $25 \pm 5\,\mathrm{emu/cm}^3$ in the $Sr_3Ru_2O_7$ layers (unless otherwise noted, all error bars and uncertainties represent ± 1 standard deviation). Such a finding has two implications. One is that the canted ferromagnetism in the bulk Sr_2IrO_4 is either zero or below the detection limit. The other implication is that the $Sr_3Ru_2O_7$ layers in the SLs transition to the ferromagnetic state at a much lower critical field than the bulk (about 7 T) [18,26]. To make a comparison, we measured the saturation magnetization using a superconducting quantum interference device (SQUID) under the same measurement conditions, and the result is about $23.5\,\mathrm{emu/cm}^3$ (see SM Sec. S7 [17]), which is consistent with the PNR result.

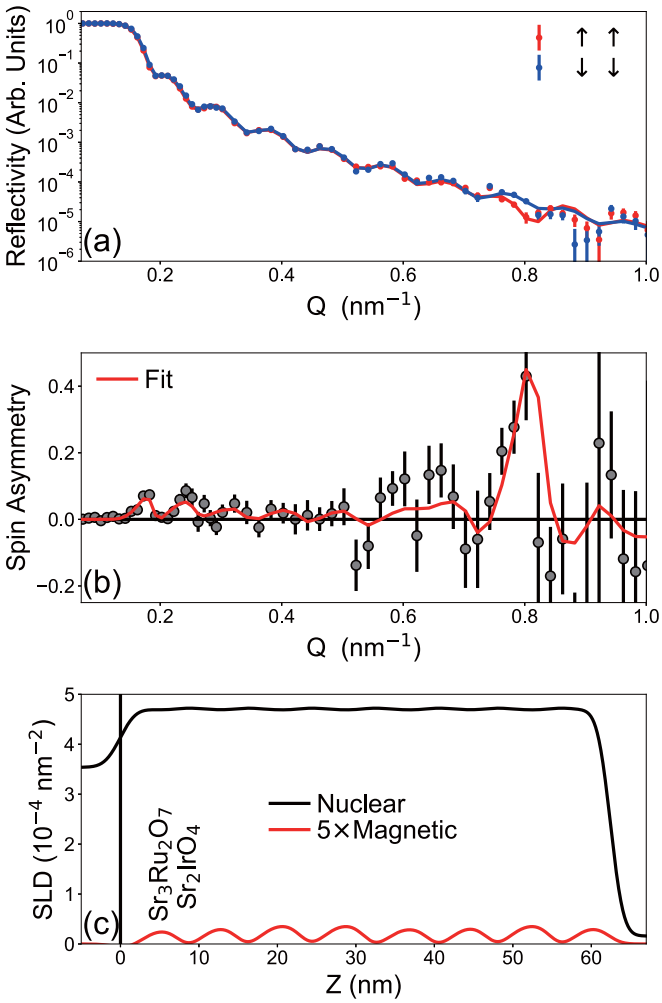

FIG. 5. (a) Polarized neutron reflectometry and (b) spin asymmetry at 5 K in an applied in-plane magnetic field of 3 T alongside simulations from the best-fit model. (c) The magnetic and nuclear depth-profile model used to generate the fits shown.

IV. DISCUSSIONS

Despite the resemblance to bulk conduction behavior above the localization temperature, we observe significant deviations at low temperatures, where the Hall resistivity of the $N = 2$ and 4 SLs exhibit different nonlinear dependences on the magnetic field from that of the $Sr_3Ru_2O_7$ film. Strikingly, the Hall resistivities of the $N = 2$, 4 SLs at 4 K exhibit abrupt downturns above the critical field of 1.3 and 2.1 T, respectively. For the $N = 2$ SL, the downturn even reverses the sign of the slope below the critical field. Such behaviors are absent in the $Sr_3Ru_2O_7$ film, which exhibits a typical anomalous Hall effect with saturating Hall resistivity near 6 T.

In order to understand the low-temperature anomalies observed in the SLs, we propose two possible schemes. One possible scheme is that electron and hole pockets coexist near the Fermi level and are absent of spin reorientation transitions. Under such a scheme, the Hall resistivity peak observed near 1.3 T in the $N = 2$ SL can be explained by the competition between hole carriers dominating the transport below the critical field and electron carriers dominating above the critical field. Usually, negative magnetoresistance is expected for ferromagnetic or weakly ferromagnetic systems because of the weak localization effect [2,27], while positive magnetoresistance is expected for nonferromagnetic systems with strong spin-orbit coupling [28]. One can make an even simpler assumption that the electron carriers are from the Sr_2IrO_4 layers, which are weakly ferromagnetic in thin films, and the hole carriers are from the $Sr_3Ru_2O_7$ layers, which are weakly ferromagnetic in the intermediate temperature range (50–150 K) and metamagnetic at low temperatures (below 50 K) in thin films. Then in the SLs much above the localization temperatures (in the range from 16 to 72 K), negative magnetoresistance is expected when either electron (from Sr_2IrO_4) or hole carriers (from $Sr_3Ru_2O_7$) are dominating the transport. Indeed, the experimental magnetoresistances of all SLs are all negative much above the localization temperatures (see Fig. 4). Below the localization temperature, the zero magnetoresistance may be understood in terms of competition between the hole's positive magnetoresistance that emerges after a nematic phase transition in the $Sr_3Ru_2O_7$ thin films and the negative magnetoresistance of electron carriers from the Sr_2IrO_4 slab, which balances so that the overall magnetoresistance is near zero [16]. However, such a simple scheme is not enough to explain the kink of the Hall resistivity [Fig. 3(b)] and the abrupt transition from zero magnetoresistance to negative magnetoresistance [Fig. 4(e)], both observed in the $N = 4$ SL at the 1.3 T critical field.

Another possible scheme to discuss is that carrier concentration, mobility, and all the other electronic freedoms are not tuned by the magnetic field but only a spin reorientation transition occurs in the critical field. The bump feature of the anomalous Hall resistivity [Fig. 3(b) inset] observed in the $N = 2$ SL shares certain similarities to the same feature that has been seen in the $SrRuO_3$ ultrathin films and heterostructures [21,29–31]. It has been attributed to the topological Hall effect [21] and later to the Berry curvature sign difference of two constituent phases [32]. Both pictures are led by the strong spin-orbit interaction. In such a scheme, the charge carriers are the same but the spin directions of conducting carriers follow a topological ordering transition [21], or the Berry curvature experiences a temperature-dependent sign change [32]. However, there are also some inconsistencies in this scheme. One inconsistency is that the pure spin transition picture fails to explain the negative slope to positive slope change of the linear ρ_{xy} vs H observed in the $N = 4$ SL [see Fig. 3(c)]. Another inconsistency is that in the $N = 2$ SL the anomalous Hall resistivity bump appears only in the field sweep starting from 0 T and is absent when the field is swept from 9 T (see SM Sec. S8 [17]).

Additionally, it is worthwhile to discuss the role of the interface. Coexisting electron and hole charges can come from the relative band offset of the two constituent layers and the associated charge transfer across the interface. Since a small amount of intermixing at the interface is expected from the XRR, the effect of Ru doping in the interfacial Sr_2IrO_4 or the iridium doping in the interfacial $Sr_3Ru_2O_7$ has to be considered. From previous studies, it is known that Ru doping in Sr_2IrO_4 induces holes, since Ru^{4+} (d^4) has one less d electron than Ir^{4+} (d^5) [33,34]. Reversely, it is possible that Ir doping

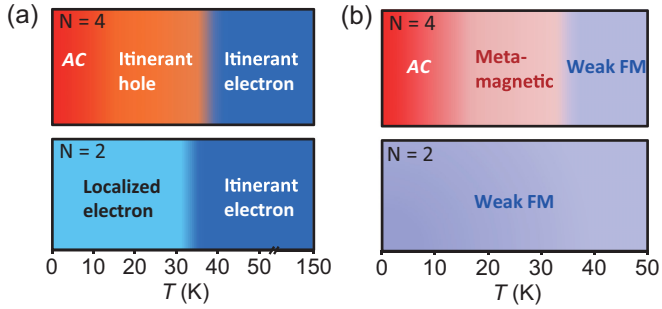

FIG. 6. The summary diagrams of the $N = 2$ and $N = 4$ SLs: (a) the charge carrier types revealed by Hall measurements and (b) the magnetism revealed by the magnetoresistance as functions of temperature (T). FM stands for ferromagnetism and AC stands for anomalous charge.

in the interfacial $Sr_3Ru_2O_7$ induces electron carriers. Thus, the electron conducting channel may be tightly confined near the interface. Furthermore, since the ferromagnetism is shown to reside only in the $Sr_3Ru_2O_7$ layers, the anomalous behaviors of both magnetoresistance (zero-to-negative transition) and the Hall resistivity peak at the critical field are suggested to be linked to the $Sr_3Ru_2O_7$ layers. But the spatial distribution of the electron and hole channels is difficult to resolve in the current study.

Finally, the overall interpretation of the experimental results of the $N = 2$ and 4 SLs is summarized into diagrams in Figs. 6(a) and 6(b). Below the localization temperature, the $N = 4$ SL exhibits an anomalous charge phase regime which is indicated by the red color in the diagrams. In this regime, charge carriers in the SLs are localized due to the two dimensionality, which is different than the metallic state of the $Sr_3Ru_2O_7$ film. The carrier type is anomalous, which might include both electrons and holes. Normally the carrier type has a very weak dependence on temperature. Moreover, the critical field dependence of the Hall resistivity has not been observed in the $Sr_3Ru_2O_7$ thin film or bulk [26,35,36]. These anomalous behaviors in the SLs cannot be explained by either the simple composite model or by a simple spin reorientation transition. Rather, the SLs are all constructed with short periods which effectively fold the Brillion zone so that the electronic structures of both component layers are strongly coupled and reconstructed.

V. CONCLUSIONS

In conclusion, we fabricated $(Sr_2IrO_4)_4/(Sr_3Ru_2O_7)_N$ ($N = 1$, 2, and 4) SLs using RHEED-assisted PLD and performed electric transport, magnetoelectric transport, and PNR measurements. The SLs are found to exhibit an electromagnetic phase diagram that is dependent on both the period and the temperature. The carrier type (electron or hole) and the conductivity (itinerant or localized) are strongly dependent on the temperature and the period. Most interestingly, we found a special localized phase regime in the $N = 4$ SL at very low temperatures in which both the magnetoresistance and the Hall resistivity exhibit an abrupt magnetic transition at the critical field, and PNR measurements identify ferromagnetism in the $Sr_3Ru_2O_7$ layers only. Our study demonstrates the SLs of heavy transition-metal oxides are a rich platform for revealing exotic types of electromagnetic phases and quantum critical phase transitions.

ACKNOWLEDGMENTS

The authors acknowledge fruitful discussions with X. Lin. This work was supported by the National Natural Science Foundation of China (Grants No. 51627901 and No. 11574287), National Key Research and Development Program of China (Grant No. 2016YFA0401004), the Fundamental Research Funds for the Central Universities (Grant No. WK2340000088), Anhui Initiative in Quantum Information Technologies (Grant No. AHY100000). X.Z. acknowledges the support of the Youth Innovation Promotion Association CAS (Grant No. 2016389). Certain commercial equipment, instruments, or materials are identified in this paper to foster understanding. Such identification does not imply recommendation or endorsement by the National Institute of Standards and Technology, nor does it imply that the materials or equipment identified are necessarily the best available.

[1] M. Salluzzo, J. C. Cezar, N. B. Brookes, V. Bisogni, G. M. De Luca, C. Richter, S. Thiel, J. Mannhart, M. Huijben, A. Brinkman, G. Rijnders, and G. Ghiringhelli, Phys. Rev. Lett. **102**, 166804 (2009).

[2] L. D. Miao, H. Xu, and Z. Q. Mao, Phys. Rev. B **89**, 035109 (2014).

[3] T. Han, Y. J. Wang, J. Yang, L. He, J. M. Xu, D. D. Liang, H. Han, M. Ge, C. Y. Xi, W. K. Zhu, C. J. Zhang, and Y. H. Zhang, Appl. Phys. Lett. **109**, 192409 (2016).

[4] Y. Hu, X. Chen, S.-T. Peng, C. Lane, M. Matzelle, Z.-L. Sun, M. Hashimoto, D.-H. Lu, E. F. Schwier, M. Arita, T. Wu, R. S. Markiewicz, K. Shimada, X.-H. Chen, Z.-X. Shen, A. Bansil, S. D. Wilson, and J.-F. He, Phys. Rev. Lett. **123**, 216402 (2019).

[5] Y. Wang, R. Wang, J. Kim, M. H. Upton, D. Casa, T. Gog, G. Cao, G. Kotliar, M. P. M. Dean, and X. Liu, Phys. Rev. Lett. **122**, 106401 (2019).

[6] K. Nishio, H. Y. Hwang, and Y. Hikita, APL Mater. **4**, 036102 (2016).

[7] C. L. Lu, A. Quindeau, H. Deniz, D. Preziosi, D. Hesse, and M. Alexe, Appl. Phys. Lett. **105**, 082407 (2014).

[8] M. Ge, T. F. Qi, O. B. Korneta, D. E. De Long, P. Schlottmann, W. P. Crummett, and G. Cao, Phys. Rev. B **84**, 100402(R) (2011).

[9] T. F. Qi, O. B. Korneta, L. Li, K. Butrouna, V. S. Cao, Xiangang Wan, P. Schlottmann, R. K. Kaul, and G. Cao, Phys. Rev. B **86**, 125105 (2012).

[10] T. F. Qi, O. B. Korneta, S. Chikara, M. Ge, S. Parkin, L. E. De Long, P. Schlottmann, and G. Cao, J. Appl. Phys. **109**, 07D906 (2011).
[11] S. T. Dong, B. B. Zhang, L. Y. Zhang, Y. B. Chen, J. Zhou, S. T. Zhang, Z. B. Gu, S. H. Yao, and Y. F Chen, Phys. Lett. A **378**, 2777 (2014).
[12] J. Nichols and H. N. Lee, *Metal Oxide-Based Thin Film Structures* (Elsevier, Amsterdam, 2018).
[13] C. Mirri, L. Baldassarre, S. Lupi, M. Ortolani, R. Fittipaldi, A. Vecchione, and P. Calvani, Phys. Rev. B **78**, 155132 (2008).
[14] R. A. Borzi, S. A. Grigera, J. Farrell, R. S. Perry, S. J. S. Lister, S. L. Lee, D. A. Tennant, Y. Maeno, and A. P. Mackenzie, Science **315**, 214 (2007).
[15] E. Fradkin, S. A. Kivelson, M. J. Lawler, J. P. Eisenstein, and A. P. Mackenzie, Annu. Rev. Condens. Matter Phys. **1**, 153 (2010).
[16] P. B. Marshall, K. Ahadi, H. Kim, and S. Stemmer, Phys. Rev. B **97**, 155160 (2018).
[17] See Supplemental Material at http://link.aps.org/supplemental/10.1103/PhysRevB.101.155151 for information on superlattices and bare films, including reciprocal space maps, rocking curves, additional fits of the resistivity, additional fits of the polarized neutron reflectivity, SQUID magnetizations, and additional Hall measurements.
[18] A. Tiwari and K. P. Rajeev, Solid State Commun. **111**, 33 (1999).
[19] J. A. N. Bruin, H. Sakai, R. S. Perry, and A. P. Mackenzie, Science **339**, 804 (2013).
[20] P. A. Lee and T. V. Ramakrishnan, Rev. Mod. Phys. **57**, 287 (1985).
[21] J. Matsuno, N. Ogawa, K. Yasuda, F. Kagawa, W. Koshibae, N. Nagaosa, Y. Tokura, and M. Kawasaki, Sci. Adv. **2**, e1600304 (2016).
[22] J. Ravichandran, C. R. Serrao, D. K. Efetov, D. Yi, Y. S. Oh, S. W. Cheong, R. Ramesh, and P. Kim, J. Phys.: Condens. Matter. **28**, 505304 (2016).
[23] S. V. Morozov, K. S. Novoselov, M. I. Katsnelson, F. Schedin, L. A. Ponomarenko, D. Jiang, and A. K. Geim, Phys. Rev. Lett. **97**, 016801 (2006).
[24] B. J. Kirby, P. A. Kienzle, B. B. Maranville, N. F. Berk, J. Krycka, F. Heinrich, and C. F. Majkrzak, Curr. Opin. Colloid Interface Sci. **17**, 44 (2012).
[25] B. Maranville, W. Ratcliff II, and P. Kienzle, J. Appl. Cryst. **51**, 1500 (2018).
[26] S. A. Grigera, R. S. Perry, A. J. Schofield, M. Chiao, S. R. Julian, G. G. Lonzarich, S. I. Ikeda, Y. Maeno, A. J. Millis, and A. P. Mackenzie, Science **294**, 329 (2001).
[27] I. N. Bhatti, R. Rawat, A. Banerjee, and A. K. Pramanik, J. Phys.: Condens. Matter **27**, 016005 (2015).
[28] M. Jenderka, J. Barzola-Quiquia, Z. P. Zhang, H. Frenzel, M. Grundmann, and M. Lorenz, Phys. Rev. B **88**, 045111 (2013).
[29] I. Lindfors-Vrejoiu and M. Ziese, Phys. Status Solidi **254**, 1600556 (2017).
[30] B. Pang, L. Zhang, Y. B. Chen, J. Zhou, S. Yao, S. Zhang, and Y. Chen, ACS Appl. Mater. Interfaces **9**, 3201 (2017).
[31] Q. Qin, L. Liu, W. Lin, X. Shu, Q. Xie, Z. Lim, C. Li, S. He, G. M. Chow, and J. Chen, Adv. Mater. **31**, 1807008 (2019).
[32] D. Kan, T. Moriyama, K. Kobayashi, and Y. Shimakawa, Phys. Rev. B **98**, 180408(R) (2018).
[33] S. J. Yuan, S. Aswartham, J. Terzic, H. Zheng, H. D. Zhao, P. Schlottmann, and G. Cao, Phys. Rev. B **92**, 245103 (2015).
[34] A. Glamazda, W. J. Lee, K. Y. Choi, P. Lemmens, H. Y. Choi, N. Lee, and Y. J. Choi, Phys. Rev. B **89**, 104406 (2014).
[35] R. A. Borzi, A. McCollam, J. A. N. Bruin, R. S. Perry, A. P. Mackenzie, and S. A. Grigera, Phys. Rev. B **84**, 205112 (2011).
[36] R. S. Perry, L. M. Galvin, A. P. Mackenzie, D. M. Forsythe, S. R. Julian, S. I. Ikeda, and Y. Maeno, Physica B **284-288**, 1469 (2000).